Equilibrium figure of a rotating body composed of two-layered incompressible fluids with application to the theory of lunar origin

T. Kubo-oka[1] **and K. Nakazawa**[2]

[1] Hydrographic Department of Japan, Tsukiji 5-3-1, Chuo-ku, Tokyo 104, Japan
[2] Earth and Planetary Sciences, Tokyo Institute of Technology, O-okayama 2-12-1, Meguro-ku, Tokyo 152, Japan

Abstract. Recent geochemical research on the bulk composition of the Moon implies that the lunar material comes from the terrestrial magma ocean. Rotational fission seems to be a favorable candidate for the mechanism to tear off the magma ocean although it has several physical difficulties. In most of the previous studies on rotational fission, the proto-Earth was treated as a single-layered body. In this study, we modeled the proto-Earth as a superposition of two layers of incompressible fluids with different densities to take into account the effect of inhomogeneity of the proto-Earth.

We first looked for the gravitational equilibrium figure of such rotating two-layered axisymmetric masses numerically. We found that, when the rotation is slow, both the body surface and the boundary between the two layers are well approximated by spheroids. As the body rotates faster, the body surface begins to deviate from a spheroid while the boundary between the two layers stays spheroidal. Furthermore, when the rotational angular momentum beyonds a certain critical value, the outward centrifugal force overcomes the inward gravitational force and the body can no longer keep a single figure.

We next investigated the stability of the equilibrium figures against small perturbations using the criterion derived by Chandrasekhar & Lebovitz (1962). For the cases where the values of the parameters are suitable for the proto-Earth, the condition of secular instability is almost the same as that for the Maclaurin spheroid. Moreover, the body reaches the critical angular momentum before dynamical instability occurs. However, the critical angular momentum is almost the same as that needed to trigger dynamical instability. Therefore, even if the inhomogeneity of the proto-Earth is taken account, rotational fission is an unlikely mechanism for lunar origin.

Key words: solar system: formation – Earth – Moon

1. Introduction

The problem of lunar origin has been a "Gordian Knot" for hundreds of years. Many hypotheses and their variants for lunar origin have been proposed since the 17th century. However, we have not established a theory which satisfies both the geochemical and the dynamical constraints.

One of the geochemical constraints of the Moon is that elements like V, Cr, and Mn are depleted in comparison to the CI chondrites. These elements are also depleted in the terrestrial mantle and the depletion factors in these bodies are similar (Ringwood and Seifert 1988). Based on experimental measurements, Ringwood et al. (1991) showed V, Cr, and Mn were not depleted in Martian-sized or smaller bodies. They also suggested that the similarity in the depletion factors for these elements is evidence that most lunar materials were derived from the proto-Earth. Moreover, Okuchi (1995) showed that the $mg^{\sharp}$ number of the Moon is identical to that of the terrestrial magma ocean which is formed at a depth of about 300 km with a temperature as high as 1600 °C. Furthermore, the abundance of the siderophile elements like Ni, Co, and W of the Moon agrees with those estimated from this model of the magma ocean. Therefore, it is natural, at least from the viewpoint of geochemical studies on lunar materials, to conclude that the lunar materials came from the magma ocean of the proto-Earth.

The giant impact hypothesis is most preferable from the dynamical point of view since it is the only hypothesis that can explain the extraordinarily large angular momentum of the Earth-Moon system. However, according to the results of numerical simulations of a giant impact (Benz et al. 1986, 1987, 1989; Cameron & Benz 1991), the material scattered around the proto-Earth comes mostly from the Mars-sized impactor. In other words, a giant impact cannot tear off the outer layer of the proto-Earth. This feature is inconsistent with the geochemical constraint.

On the other hand, the rotational fission hypothesis is most preferable from the geochemical point of view since it is the only hypothesis that can tear off the outer part of the proto-Earth. However, from the dynamical point of view, this hypothesis has

several disadvantages (see e.g. Boss & Peale 1986). The most crucial disadvantage is the problem of the angular momentum. In order for rotational fission to take place, the total angular momentum must be about 4 times larger than that of the present Earth-Moon system. Furthermore, after the fission process is complete, the excess angular momentum has to be consumed by ejecting material from the Earth-Moon system.

In most previous studies about rotational fission, the proto-Earth was treated as a single-layered body composed of an incompressible fluid (see e.g. Chandrasekhar 1969). However, as a result of core formation, the proto-Earth becomes no longer homogeneous. Thus, the effect of inhomogeneity of the proto-Earth must be taken into account.

There are two different approaches to the problem: one is to assume an arbitrarily continuous density distribution. Durisen & Scott (1984) dealt with inviscid polytropic fluids and investigated the fission process after the onset of dynamical instability. Their results show that the materials are sprayed around the central body and the angular momentum needed to trigger the fission is almost same as that for a homogeneous body. Boss (1986) simulated the evolution of a uniformly rotating, axisymmetric, viscous polytropic body with $n = 1/2$ after a sudden increase in the rotational angular velocity. The value of the polytropic index corresponds approximately to the compressibility of the Earth. He found that the body begins to lose materials from its equator before reaching dynamical instability. The material released from the body forms a torus and moves outward. This phenomenon is called "mass-shedding".

A different and more quantitative approach is to treat the proto-Earth as the superposition of several incompressible fluids with different densities. In this paper, we will adopt this approach and suppose that the proto-Earth is composed of two layers. Hereafter, we call these layers 'mantle' and 'core' for convenience. The main purpose of this paper is to clarify when an instability which leads to fission of the rapidly rotating body can occur for the case where the inhomogeneity of the proto-Earth is taken into account. To investigate stability, we first seek for an equilibrium figure of the body assuming that it is axisymmetric with respect to the rotational axis. By the use of the linear perturbation method, we next examine the stability of the equilibrium figure against small perturbations.

In Sect. 2, we will show the numerical procedure used to find equilibrium figures of the two-layered incompressible bodies. Our method is an extension of the method developed by Eriguchi & Sugimoto (1981). The equilibrium figures, obtained numerically for various ranges of parameters, will be described in Sect. 3. Section 4 will determine the stability of the equilibrium figures based on the criterion derived by Chandrasekhar & Lebovitz (1962). Application to the lunar origin will be discussed in Sect. 5.

2. Basic formulation

Suppose that a gravitating system with uniform rotation is composed of two layers with different density. Hereafter, these two layers will be called the mantle and the core. The volumes of the
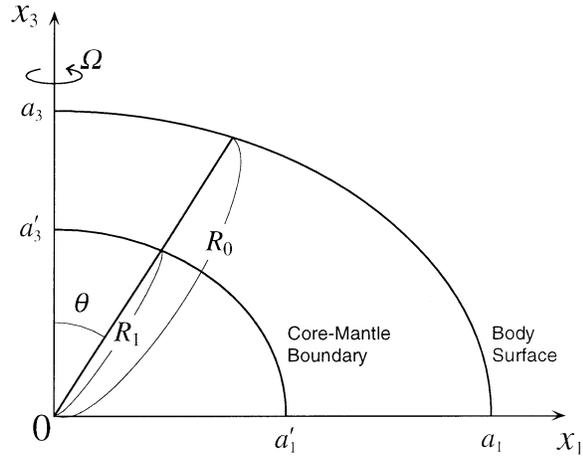

Fig. 1. Geometrical configuration of the system. Here, a_1, a_3, a'_1, and a'_3 are the equatorial and the polar radius of the body surface and the equatorial and the polar radius of the core-mantle boundary, respectively.

whole body and the core are denoted by V_0 and V_1. A schematic picture of the body is illustrated in Fig. 1 together with the adopted coordinates. The coordinate system is identical to that adopted by Chandrasekhar and Lebovitz (1962). In the present study, we have made the following assumptions for simplicity:

1. Both the mantle and the core consists of incompressible fluids whose densities are ρ_0 and ρ_1 ($\rho_1 > \rho_0$), respectively.
2. The rotational angular velocity Ω is constant throughout the body.
3. The equilibrium figure is axisymmetric and plane-symmetric with respect to the rotation axis and the equatorial plane, respectively.

In the present study we use the spherical polar coordinates (r, θ, φ) whose origin is placed at the center of mass of the body. Owing to assumption 3, the body surface and the core-mantle boundary can be completely determined by r and μ ($= \cos \theta$). Namely, the body surface and the core-mantle boundary are described by the following:

$$\begin{cases} r = R_0(\mu) & \text{at the body surface,} \\ r = R_1(\mu) & \text{at the core-mantle boundary.} \end{cases} \tag{1}$$

Here, we assume that R_0 and R_1 are single-valued and monotonically decreasing functions of μ. For the sake of later convenience, we introduce the two following quantities:

$$\epsilon = \sqrt{1 - (a_3/a_1)^2} \,, \tag{2}$$

and

$$\eta = a'_1/a_1 \,, \tag{3}$$

where a_1, a_3, a'_1 are the equatorial radius of the body surface, the polar radius of the body surface, and the equatorial radius of the core-mantle boundary, respectively (see Fig. 1). If the figure of the body surface is spheroidal, ϵ coincides with the

eccentricity of the spheroid. Hereafter, ϵ is referred to as "the coaspect ratio" for simplicity.

The gravitational potential $\Phi_g(r, \mu)$ can be described by the sum of the potentials Φ_{g0} and Φ_{g1}: the former is due to a body with density ρ_0 and volume V_0 and the latter is due to a body with density $\rho_1 - \rho_0$ and volume V_1. Namely, we have

$$\Phi_g(r, \mu) = \Phi_{g0}(r, \mu) + \Phi_{g1}(r, \mu) , \qquad (4)$$

where

$$\frac{\Phi_{g0}(r, \mu)}{4\pi G \rho_0} = \qquad (5)$$

$$\sum_{n=0}^{\infty} P_{2n}(\mu) \int_0^1 d\mu' P_{2n}(\mu') h(r, R_0(\mu'); n)$$

and

$$\frac{\Phi_{g1}(r, \mu)}{4\pi G \rho_0} = \qquad (6)$$

$$\frac{\rho_1 - \rho_0}{\rho_0} \sum_{n=0}^{\infty} P_{2n}(\mu) \int_0^1 d\mu' P_{2n}(\mu') h(r, R_1(\mu'); n) ,$$

where $P_{2n}(\mu)$ is the Legendre polynomials of rank $2n$. In the above, $h(r, r'; n)$ is a function defined by

$$
\begin{aligned}
&h(r, r'; n) \\
&= \begin{cases}
\frac{1}{2n+3} \frac{r'^{2n+3}}{r^{2n+1}} & \text{for } r \leq r', \\
\frac{(4n+1)r^2}{(2n+3)(2n-2)} - \frac{1}{2n-1} \frac{r'^{2n+3}}{r^{2n+1}} & \text{for } r < r' \text{ and } n \neq 1, \\
r^2(\frac{1}{5} + \ln \frac{r'}{r}) & \text{for } r < r' \text{ and } n = 1.
\end{cases}
\end{aligned}
\qquad (7)
$$

The centrifugal potential Φ_c is simply given by

$$\Phi_c(r, \mu, \Omega) = \Omega^2 \frac{r^2 (1 - \mu^2)}{2} . \qquad (8)$$

Gravitational equilibrium is achieved when the total potential Φ_t, i.e., the sum of the gravitational potential $\Phi_g(r, \mu)$ and the centrifugal potential $\Phi_c(r, \mu, \Omega)$, is constant at the body surface as well as at the core-mantle boundary. Therefore, R_0 and R_1 must satisfy the following conditions:

$$\Phi_{g0}(R_0, \mu) + \Phi_{g1}(R_0, \mu) + \Phi_c(R_0, \mu, \Omega) = C_0 \qquad (9)$$

and

$$\Phi_{g0}(R_1, \mu) + \Phi_{g1}(R_1, \mu) + \Phi_c(R_1, \mu, \Omega) = C_1 , \qquad (10)$$

where C_0 and C_1 are constants. These are the equilibrium equations to be solved.

To find the solution to Eqs. (9) and (10) numerically, we divide the coordinate region of the colatitude (i.e., cosine of the colatitude, μ) into $N + 1$ points with an equal interval:

$$\mu_j = \frac{j}{N}, \qquad j = 0, 1, \ldots, N. \qquad (11)$$

Then, we will denote the corresponding radial distances of the body surface and the core-mantle boundary as

$$R_k^{(j)} = R_k(\mu_j) \qquad k = 0 \text{ or } 1, \qquad (12)$$

where $k = 0$ and $k = 1$ mean, respectively, the values at the body surface and at the core-mantle boundary. For the sake of numerical convenience, the equatorial radius of the body is chosen to be

$$R_0^{(0)} = 1. \qquad (13)$$

In Eqs. (9) and (10), unknown quantities are $R_0^{(j)}$ ($j = 1$ to N), $R_1^{(j)}$ ($j = 0$ to N), Ω, C_0, and C_1 and the number of them is $2N+4$ while the number of equations is $2N+2$. So, if two of the unknown quantities are given as parameters, then we can solve the equations. We choose ϵ and η as the two parameters, which are defined by Eqs. (2) and (3), respectively: in the present case ϵ and η are rewritten, respectively, by

$$\epsilon = \sqrt{1 - \left(R_0^{(N)}\right)^2} \qquad (14)$$

and

$$\eta = R_1^{(0)} \qquad (15)$$

since $R_0^{(0)}$ is chosen to be 1.

To find the solutions we use a Newton-Raphson iteration scheme:

1. We first assume the tentative values of R_0^j, R_1^j, Ω^2, C_0, and C_1, which are denoted by R_0^{j0}, R_1^{j0}, $(\Omega^2)^0$, C_0^0, and C_1^0, respectively.
2. We substitute $R_0^j = R_0^{j0} + \delta R_0^j$, $R_1^j = R_1^{j0} + \delta R_1^j$, $(\Omega^2) = (\Omega^2)^0 + \delta(\Omega^2)$, $C_0 = C_0^0 + \delta C_0$, and $C_1 = C_1^0 + \delta C_1$ into Eqs. (9) and (10) and retain only the first order terms such as δR_0^j, δR_1^j, etc.
3. Next we solve the simultaneous algebraic equations of order $2N+2$ by means of a standard matrix inversion method and find δR_0^j, δR_1^j, etc.
4. Further we replace R_0^{0j}, R_1^{0j}, etc. by $R_0^{0j} + \delta R_0^j$, $R_1^{0j} + \delta R_1^j$, etc. and return to step 2 until δR_0^j, δR_1^j, etc. become sufficiently small.

We truncate the above procedure when the condition

$$\text{Max} \left[\frac{\delta R_0^j}{R_0^{0j}}, \frac{\delta R_1^j}{R_1^{0j}}, \frac{\delta(\Omega^2)}{(\Omega^2)^0}, \frac{\delta C_0}{C_0^0}, \frac{\delta C_1}{C_1^0} \right] < 10^{-4} \qquad (16)$$

is satisfied.

In the present study, the number of divisions N in μ (see Eq. 11) is taken to be 160. To check the accuracy of numerical calculations, we examined the case of $N = 320$ for several sets of ϵ and η and found that there were no obvious differences in the results between the cases of $N = 160$ and 320. In many cases, we can arrive at a solution within five iterations. In the evaluation of the potentials, we use Simpson's method for the integration with respect to μ' and take the first 25 terms (at most) for the summation over n; more exactly, $n = 15$ for the case of $\epsilon \leq 0.8$ and $n = 25$ for the case of $\epsilon > 0.8$.
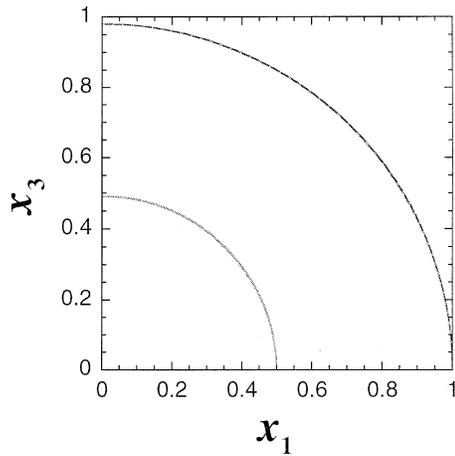
Fig. 2. Meridional cross section for the case of $\epsilon = 0.2$. The spheroidal surfaces with the same semimajor axis and coaspect ratio are also plotted by dashed curves. In this case, both the body surface and the core-mantle boundary coincide with these spheroidal surfaces.

Fig. 3. The same as Fig. 2, but for the case where $\epsilon = 0.9$.

As explained above, the parameters given in the calculation are ϵ and η. However, we are interested in solutions with a definite volume ratio $(V_1/V_0)^*$. So, we evaluate the volume ratio V_1/V_0 after the equilibrium figure is obtained for a fixed value of ϵ and a tentative value of η. If the evaluated ratio V_1/V_0 does not coincide with $(V_1/V_0)^*$, then we repeat the calculations changing η by $1/100$, until we find the largest value of η satisfying the inequality $V_1/V_0 < (V_1/V_0)^*$ and the smallest η satisfying the inequality $(V_1/V_0)^* < V_1/V_0$. Then, evaluating the value of η which gives the desired volume ratio by means of linear interpolation, we finally find the equilibrium figure for a desired set of ϵ and $(V_1/V_0)^*$.

3. Equilibrium figures of two-layered bodies

First, we will concentrate on the equilibrium figures of slowly rotating bodies. Hereafter, unless we note explicitly, the volume ratio V_1/V_0 and the density ratio ρ_1/ρ_0 are taken to be $1/8$ and 2, respectively. The meridional cross section of the equilibrium figure (i.e., the figure in the x_1-x_3 plane) is shown in Fig. 2 for the case where the coaspect ratio ϵ is equal to 0.2. The spheroidal surfaces with the same semimajor axis and coaspect ratio (in this case, the eccentricity of the spheroid) are also plotted by the dashed curves in Fig. 2. In this case, both the figures of the body surface and the core-mantle boundary coincide with these dashed curves. In other words, when the rotation is slow, the figures of these two boundaries are well fitted by spheroids.

When ϵ exceeds 0.8, the difference between the figure of the body surface and the spheroid with the eccentricity $e_0 = \epsilon$ becomes somewhat apparent. As ϵ increases further, the difference between the body surface and the spheroid becomes more distinct (see Fig. 3 for the case of $\epsilon = 0.9$). We can see from this figure that the actual body surface is always under the spheroidal surface with the same eccentricity ϵ (dotted curve). Furthermore, it is interesting to note that the figure of the core-mantle boundary is adequately approximated by the spheroidal
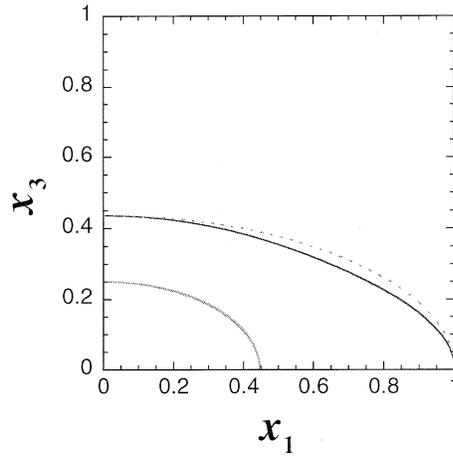
surface. This is due to the fact that the centrifugal force acts more effectively on the body surface than on the core-mantle boundary.

We find an interesting physical phenomenon which occurs between $\epsilon = 0.941$ and $\epsilon = 0.942$. The meridional cross sections obtained numerically are shown in Fig. 4. From the geometrical point of view, the cross sections in both cases have generally the same features: the body surface deviates from a spheroidal surface and behaves almost as a cusp in the vicinity of the equator. However, from the dynamical point of view, there is a crucial difference between these two cases. To clarify the difference, we draw your attention to the total potential Φ_t along the equatorial plane, which is shown in Fig. 5. For the case of $\epsilon = 0.941$, Φ_t is a monotonically increasing function of x_1 in the region $x_1 \leq 1$. For the case of $\epsilon = 0.942$, there is a point where $\partial\Phi_t/\partial x_1 = 0$ inside the body. Outside the point, $\partial\Phi_t/\partial x_1$ becomes negative, i.e., the total force acts toward the direction of positive x_1. In this region of x_1, the outward centrifugal force overcomes the inward gravitational force. Hereafter, we call the point on the x_1-axis, which satisfies $\partial\Phi_t/\partial x_1 = 0$, "the neutral point". It is natural to consider that a stable and single gravitating body cannot include a neutral point inside the body surface. In this sense, the solution for the case of $\epsilon = 0.942$ does not correspond to a single body.

Therefore, there exists a critical value of the coaspect ratio ϵ beyond which we have no equilibrium configuration as a single body with the following geometrical features:

1. Axially symmetric with respect to its rotational axis,
2. Symmetry with respect to its equatorial plane,
3. The body surface R_0 and the core-mantle boundary R_1 being single-valued and monotonically decreasing functions of μ.

Such a coaspect ratio will be called the critical coaspect ratio and denoted by ϵ_c. Note that, of course, existence of ϵ_c does not mean that any type of the equilibrium figures, e.g., triaxial figures, toroids, and others, cannot exist. From the above argument, we
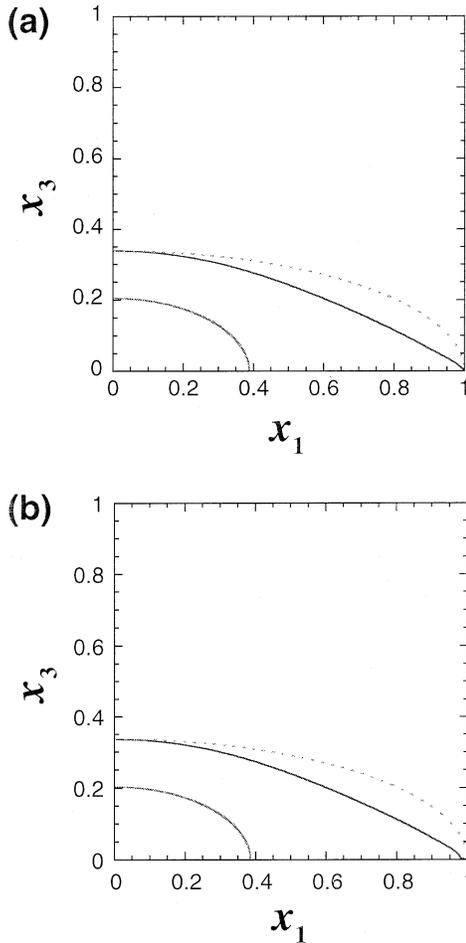
(a)

(b)

Fig. 4. a Meridional cross section for the case of $\epsilon = 0.941$. The dashed curves denote the spheroidal surfaces with the same semimajor axis and coaspect ratio. **b** The same as figure **a** but for the case where $\epsilon = 0.942$.
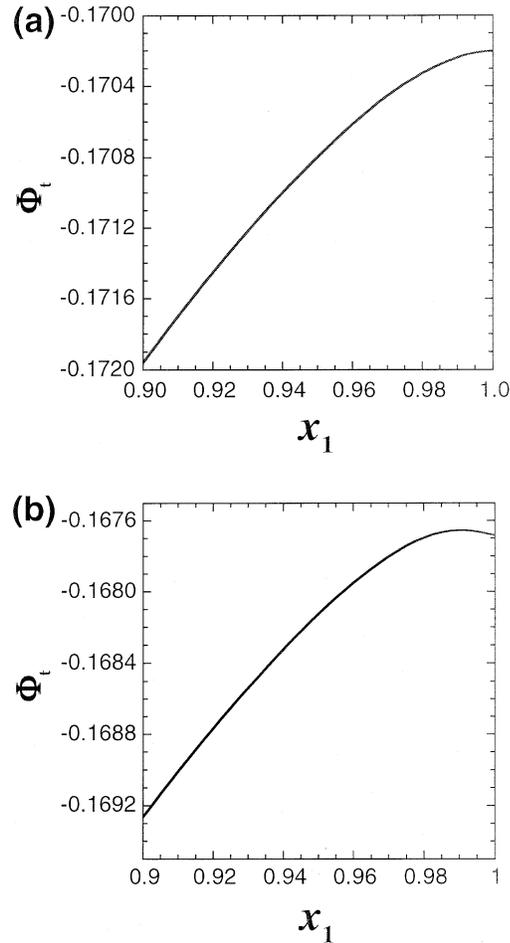
(a)

(b)

Fig. 5. a The variation of the total potential Φ_t along the x_1-axis for the case where $\epsilon = 0.941$. **b** The same as Fig. **a** but for $\epsilon = 0.942$.

can readily find the condition which gives the critical coaspect ratio ϵ_c: when

$$\frac{\partial \Phi_t}{\partial x_1} = 0 \qquad \text{at } (x_1, x_3) = (1, 0) \tag{17}$$

is satisfied for a gravitating body, then we regard such a body as corresponding to the model with just the critical coaspect ratio ϵ_c.

In Fig. 6, we show the relation between the square of the angular velocity Ω^2 and the coaspect ratio ϵ for various values of ρ_1/ρ_0. The rotational angular velocity Ω is scaled by the unit of $(\pi G \overline{\rho})^{1/2}$ where $\overline{\rho}$ is the mean density of the body:

$$\overline{\rho} = \rho_0 \left(1 + \frac{\rho_1 - \rho_0}{\rho_0} \frac{V_1}{V_0} \right). \tag{18}$$

The volume ratio V_1/V_0 is still taken to be $1/8$. The curve labeled by 1 denotes the $\Omega^2 - \epsilon$ relation of the Maclaurin spheroid (e.g., Chandrasekhar 1961), $\rho_1 = \rho_0$. The curves are terminated at the critical coaspect ratios ϵ_c which are marked by the cross '×'. For a fixed value of ϵ, $\Omega^2/\pi G \overline{\rho}$ increases with an increase in

ρ_1/ρ_0. This tendency can be explained as follows: as the degree of central condensation of mass increases under the constraint of constant mean density $\overline{\rho}$, the surface gravity at the equator becomes larger and, as a result, a stronger centrifugal force, i.e., a higher angular velocity Ω, is needed to maintain the same coaspect ratio of the equilibrium figure. As seen from this figure, ϵ_c seems to decrease with increasing ρ_1/ρ_0.

The rotational angular momentum L at equilibrium is shown in Fig. 7 for various values of the parameters ϵ and ρ_1/ρ_0. Again, the volume ratio V_1/V_0 is taken to be $1/8$. The definition of normalization constant is given by

$$\widetilde{L} = \frac{L}{(GM^3 \, \overline{a})^{1/2}}, \tag{19}$$

where M is the total mass of the body and $\overline{a}$ is the radius of the sphere which has a mass M and a mean density $\overline{\rho}$. This unit is equal to the angular momentum of a grazing satellite with mass M orbiting circularly around the body. Unlike the case of the angular velocity, for a fixed value of ϵ the normalized angular momentum $\widetilde{L}$ decreases with increasing ρ_1/ρ_0 but the difference is very small. This comes from the fact that the decrease in the moment of inertia due to mass concentration almost exactly
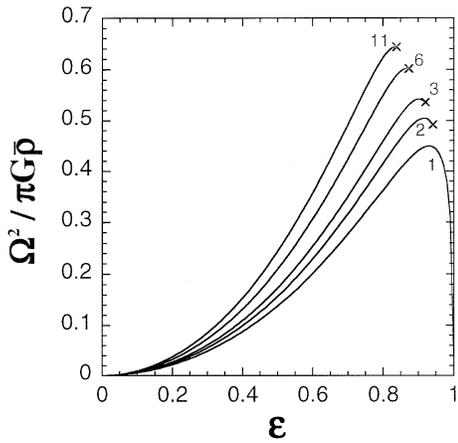
Fig. 6. The variation of the square of the angular velocity Ω plotted against the coaspect ratio ϵ for various values of ρ_1/ρ_0. The value of V_1/V_0 is taken to be 1/8. The curves are labeled by the values of ρ_1/ρ_0 and terminated at the critical coaspect ratio ϵ_c which is indicated by the cross "×". The curve labeled by 1 corresponds to the Maclaurin spheroid.
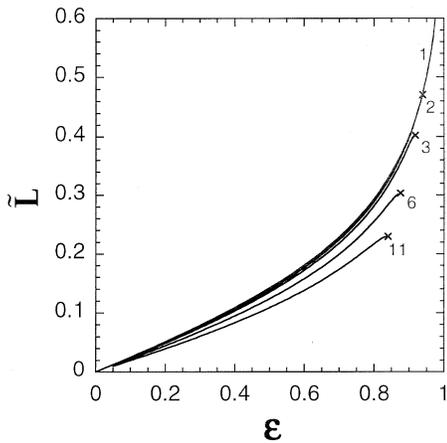

Fig. 7. The normalized angular momentum $\widetilde{L}$ (as for the normalization, see text) plotted against the coaspect ratio ϵ for various values of ρ_1/ρ_0. The value of V_1/V_0 is taken to be 1/8. The curves are labeled by the values of ρ_1/ρ_0 and terminated at the critical coaspect ratio ϵ_c which is indicated by the cross "×". The curve labeled by 1 corresponds to the Maclaurin spheroid.

cancels the increase in the angular velocity as long as $\rho_1 - \rho_0$ is relatively small.

Now, let us try to find the critical coaspect ratio ϵ_c for the cases of various values of V_1/V_0 and ρ_1/ρ_0. First, consider the limit of $\rho_1/\rho_0 \rightarrow 1$. This limit corresponds to the case of a homogeneous body, i.e., to the case of the Maclaurin spheroid. The derivative of the total potential Φ_t with respect to x_1 is given by

$$\frac{1}{\pi G \rho_0} \frac{\partial \Phi_t}{\partial x_1} = \tag{20}$$
$$\frac{4\sqrt{1-\epsilon^2}}{\epsilon^2} \left[(2-\epsilon^2)\frac{\sin^{-1}\epsilon}{\epsilon} - 2\sqrt{1-\epsilon^2} \right] x_1 \, .$$

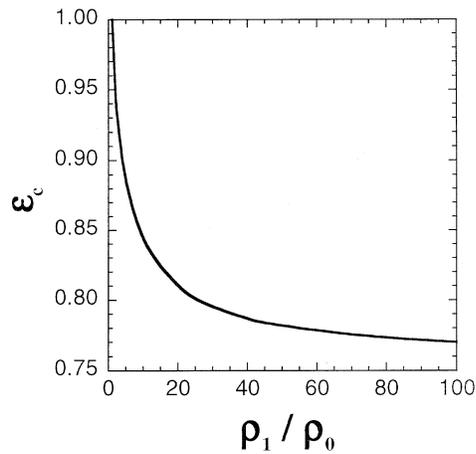**Fig. 8.** The critical coaspect ratio ϵ_c as a function of the value of ρ_1/ρ_0. The value of V_1/V_0 is taken to be 1/8.
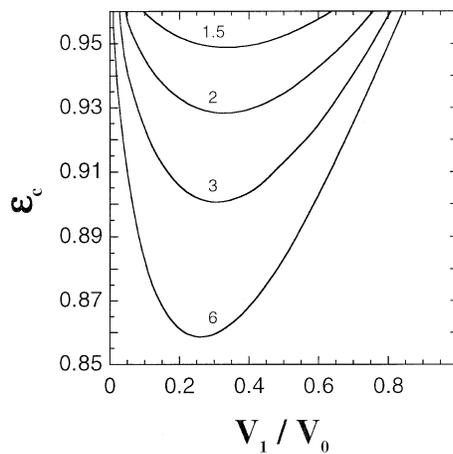

Fig. 9. The critical coaspect ratio ϵ_c as a function of the value of V_1/V_0. The curves are labeled by the values of ρ_1/ρ_0.

where we used Maclaurin's formula (e.g., Chandrasekhar 1961). Since the function of ϵ enclosed by brackets is always positive in the range where $0 < \epsilon < 1$, the right hand of Eq. (20) is always positive. Therefore, in the limit of $\rho_1/\rho_0 \rightarrow 1$ we have

$$\epsilon_c \rightarrow 1 \, . \tag{21}$$

Similarly, in the limit of $V_1/V_0 \rightarrow 0$ as well as the limit of $V_1/V_0 \rightarrow 1$, we find the same result since the body becomes homogeneous in such limits.

Using criterion (17), we can find the critical value ϵ_c numerically for various parameters V_1/V_0 and ρ_1/ρ_0. In Fig. 8, the relation between ϵ_c and ρ_1/ρ_0 is shown in the case of $V_1/V_0 = 1/8$. The value of ϵ_c decreases as ρ_1/ρ_0 increases and it tends to a certain limiting value in ϵ_c for the case of $\rho_1/\rho_0 \rightarrow \infty$. This tendency can be found for other values of V_1/V_0. We also illustrate the relation between ϵ_c and V_1/V_0 in Fig. 9. The value of ϵ_c becomes lowest at an intermediate value of V_1/V_0. This is a reasonable result since the bodies with $V_1/V_0 \ll 1$ and $V_1/V_0 \sim 1$ correspond to the Maclaurin spheroid.

If the density of the core is much larger than that of the mantle, the body can be regarded as a "core" with density ρ_1 surrounded by an "atmosphere" with very low density, ρ_0. In this case, the gravitational potential is governed only by the "core" and the figure of the "core" is that of a Maclaurin spheroid. The figure of the "atmosphere" with the critical coaspect ratio ϵ_c can be determined by the following two conditions:

1. The surface of the "atmosphere" reaches the neutral point on the equatorial plane.
2. The total potential Φ_t is constant throughout the surface of the "atmosphere".

In this case, the derivative of the the total potential Φ_t with respect to x_1 at the point $(x_1, 0, 0)$ is given by

$$\frac{1}{\pi G \rho_1} \frac{\partial \Phi_t}{\partial x_1} = -\frac{\Omega^2}{\pi G \rho_1} x_1 \tag{22}$$

$$+ \sqrt{1 - e_1^2} \left\{ \frac{x_1}{a_1' e_1^2 \sqrt{x_1^2 - a_1'^2 e_1^2}} \right.$$

$$\left. - \frac{2a_1'(1 - x_1^2/2a_1'^2 e_1^2)}{x_1^2 \sqrt{1 - a_1'^2 e_1^2/x_1^2}} - \frac{2x_1 \sin^{-1}(a_1' e_1/x_1)}{a_1'^2 e_1^3} \right\} .$$

where a_1' and e_1 are the equatorial radius and the eccentricity of the "core". Demanding $\partial \Phi_t / \partial x_1 = 0$ and noting that Ω^2 is determined by Maclaurin's formula, we can find the equatorial radius of the "atmosphere", x_1, by use of Newton-Raphson method for an arbitrary value of the eccentricity of the "core", e_1. After that, we readily draw the equi-potential surface, i.e., the surface of the "atmosphere", which passes through the neutral point. Then, the volume ratio V_1/V_0 and ϵ_c can be calculated. Repeating this procedure for various e_1, we obtain the relation between ϵ_c and the volume ratio. The results are shown in Fig. 10. From this figure, the limiting value of ϵ_c for the case where $V_1/V_0 = 1/8$ is found to be

$$\epsilon_c \to 0.756 . \tag{23}$$

4. Stability of the equilibrium figure

Suppose a mass element located at $\mathbf{x}$ in the unperturbed state is displaced slightly to $\mathbf{x} + \xi$. Here, we assume that the displacement $\xi = (\xi_1, \xi_2, \xi_3)$ can be represented by the form

$$\begin{cases} \xi_1 = \{X_{11}x_1 + X_{12}x_2\} e^{-i\sigma t} , \\ \xi_2 = \{-X_{11}x_2 + X_{12}x_1\} e^{-i\sigma t} , \\ \xi_3 = 0 . \end{cases} \tag{24}$$

where X_{ik} are constants and σ is the frequency of the perturbation. This mode corresponds to the deformation that elongates or shortens the axisymmetric body in the horizontal direction. Generally, azimuthal dependence of the nonaxisymmetric perturbations can be written as $\exp(im\phi)$ where m is an integer and ϕ is azimuthal angle (e.g. Imamura et al., 1985). The perturbation considered here corresponds to the $m = 2$ mode and is called "bar mode". According to Chandrasekhar & Lebovitz (1962), when the condition
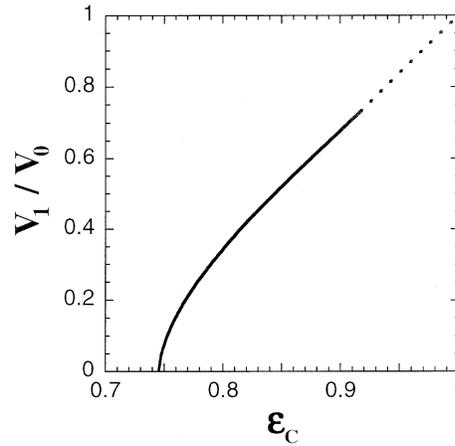
$$\Omega^2 = W_{12;12}/I_{11} \tag{25}$$

Fig. 10. The critical coaspect ratio ϵ_c plotted against the volume ratio V_1/V_0 in the limit of $\rho_1/\rho_0 \to \infty$.

is satisfied, then the characteristic root σ becomes zero and the figure is neutral against such perturbations. This corresponds to the point of secular instability. At this point, a triaxial configuration has lower total energy than an axisymmetric one. Thus, if a suitable dissipative mechanism like viscosity works, the axisymmetric configuration will evolve toward the triaxial configuration on a dissipative time scale which is considered to be very long. In the above, $W_{ij;kl}$ is a super-matrix defined by

$$W_{ij;kl} = \int_V \rho x_i \frac{\partial U_{ij}}{\partial x_l} d\mathbf{x} , \tag{26}$$

where

$$\frac{U_{ij}}{\pi G \rho_0} = \int_{V_0} \frac{(x_i - x_i')(x_j - x_j')}{|\mathbf{x} - \mathbf{x}'|^3} d\mathbf{x}' . \tag{27}$$

Furthermore, I_{ij} is the moment of inertia tensor defined by

$$I_{ij} = \int_V \rho(\mathbf{x}) x_i x_j d\mathbf{x} . \tag{28}$$

Moreover, when the condition

$$\Omega^2 I_{11} > 2 W_{12;12} \tag{29}$$

is satisfied, then σ becomes complex and the amplitude of the perturbation grows with time. In such a case, the figure is unstable against linear oscillations. This corresponds to the point of dynamical instability. If the rotational angular momentum further increases, materials of the outer layer would be ejected to form a disk around the body as Durisen and Gingold (1986) simulated numerically for polytropic bodies. Unlike the case of secular instability, dynamical instability is considered to proceed on a few rotational periods.

The stability analysis mentioned above is not complete since the mode of perturbation is artificially limited to a bar mode (Eq. 24). In fact, Friedman (1983) showed that homogeneous uniformly rotating bodies become secularly unstable against higher mode ($m > 3$) perturbations and the angular momentum

at which secular instability sets in is smaller than that for bar mode ($m = 2$). However, the growth time of secular instability increases rapidly as m increases and as the density of the body decreases. Thus, in the case of the proto-Earth, higher modes ($m > 3$) may not be effective. On the other hand, Tassoul (1978) pointed out that the condition (25) is merely an approximate one for the case of centrally condensed bodies and found that the bifurcation to a triaxial figure may occur when Ω^2 is less than $W_{12;12}/I_{11}$. In fact, polytropic bodies become secularly unstable at lower angular momentum than that for the inhomogeneous bodies (e.g., Imamura et al. 1985, 1995). So, it would be safe to regard the condition (25) as a *sufficient condition* for the onset of the secular instability for centrally condensed bodies. However, we can expect that the above-mentioned stability analysis gives the criterion, at least approximately, since the degree of central condensation of mass is relatively small (compared with a star with polytropic index $n = 3$ where the central density could be, for example, about 50 times as large as the mean density). So we will apply the method of Chandrasekhar & Lebovitz (1962) to our present stability analysis.

Since the body considered here is symmetric not only about its rotational axis but also about its equatorial plane, the supermatrix $W_{12;12}$ can be rewritten, using the cylindrical coordinates (ϖ, φ, z), as

$$W_{12;12} = \frac{\pi}{2} \int_0^{z_0} \int_0^{\varpi_0} \rho \left\{ -GD + G\varpi \frac{\partial D}{\partial \varpi} - 3\varpi^2 \frac{\partial \Phi_g}{\partial \varpi} \right.$$
$$\left. + G\varpi^2 \frac{\partial^2 D}{\partial \varpi^2} - \varpi^3 \frac{\partial^2 \Phi_g}{\partial \varpi^2} \right\} d\varpi dz , \tag{30}$$

where subscript "0" indicates the value at the body surface (Tassoul & Ostriker 1968). In the above, $\Phi_g(\mathbf{x})$ denotes the gravitational potential and $D(\mathbf{x})$ is the potential function given by

$$D(\mathbf{x}) = \int_V \rho(\mathbf{x}') \frac{\varpi' \cos(\varphi - \varphi')}{|\mathbf{x} - \mathbf{x}'|} d\mathbf{x}'$$
$$= 4\pi \sum_{k=0}^{\infty} \frac{P_{2k+1}^1(\mu)}{4k+3} \tag{31}$$
$$\int_0^1 d\mu' f(r, \mu'; k) \rho(\varpi, z) \left\{ P_{2k}(\mu') - P_{2k+2}(\mu') \right\} .$$

where P_{2k+1}^1 is the Legendre associated function and $f(r, \mu; k)$ is a function defined by

$$f(r, \mu; k) = \tag{32}$$
$$\begin{cases} \frac{(4k+3)r^3}{(2k+5)(2k-2)} - \frac{1}{2k-2} \frac{r^{2k+1}}{R(\mu)^{2k-2}} & \text{for } r < R \text{ and } n \neq 1, \\ \frac{r^3}{7} + r^3 \left(\log R(\mu) - \log r \right) & \text{for } r < R \text{ and } n = 1, \\ \frac{1}{r^{2k+5}} \frac{R(\mu)^{2k+5}}{2k+5} & \text{for } r \geq R. \end{cases}$$

In order to evaluate the double integral (30), we have to know the potentials $\Phi_g(\mathbf{x})$ and $D(\mathbf{x})$ and their derivatives with respect to ϖ at an internal point of the body. Following our treatment of gravitational potential $\Phi_g(\mathbf{x})$, we describe the potential function $D(\mathbf{x})$ as a sum of the potential functions D_0 and D_1: the former
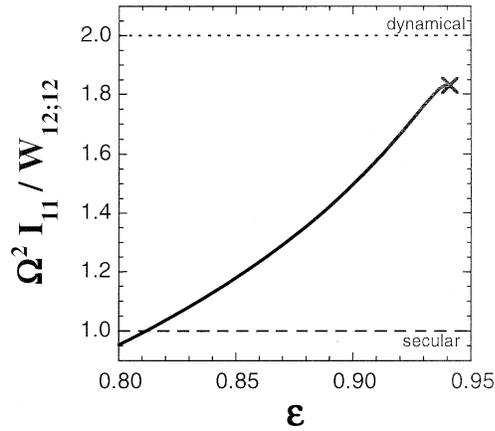

Fig. 11. The ratio $W_{12;12}/\Omega^2 I_{11}$ plotted against the coaspect ratio ϵ. The values of ρ_1/ρ_0 and V_1/V_0 are taken to be 2 and 1/8, respectively. The symbol "×" corresponds to the critical aspect ratio. The dashed and dotted horizontal lines denote, respectively, the positions where secular instability and dynamical instability begin.

is due to a body with density ρ_0 and volume V_0 and the latter is due to a body with density $\rho_1 - \rho_0$ and volume V_1.

To evaluate the potentials $\Phi_g(\mathbf{x})$ and $D(\mathbf{x})$, we divide the meridional cross section of the equilibrium figure into a number of grids: In the x_3-direction, we divide the region with a constant interval. In the x_1-direction, the segment between the rotational axis and the surface is divided into equal parts. Thus, the interval along the x_1 axis depends on x_3. To minimize the error of the calculated potential, we subdivide the grid near the pole where $x_3 > 0.8$ a_3 (a_3 being the semiminor axis of the figure). Maximum numbers of grid points in the x_1- and x_3-direction are taken to be 100 (equator) and 100 (rotational axis), respectively. The Legendre polynomials and the Legendre associated polynomials used in the calculation of the potential are taken up to the rank of 40 and 39, respectively. We used Newton's differentiation formula for the evaluation of derivatives with respect to ϖ at the grid points and Simpson's method for the numerical integrations over μ, ϖ, and z.

In Fig. 11 we show the variation of the ratio of the supermatrix $W_{12;12}$ to $\Omega^2 I_{11}$ plotted against the coaspect ratio ϵ for the case where $\rho_1/\rho_0 = 2$ and $V_1/V_0 = 1/8$. The curve is terminated at the point (marked by the cross ×) where ϵ is equal to the critical coaspect ratio ϵ_c. The dashed horizontal line denotes the position where the criterion for secular instability is satisfied. From Fig. 11, we find that the solid curve intersects the dashed curve at the point where

$$\epsilon_s \sim 0.812 . \tag{33}$$

In the above, the subscript 's' denotes the secular instability point. This value coincides with that of the Maclaurin spheroid $\epsilon_s = 0.81267$ to within the accuracy of our calculation. The dotted horizontal line denotes the position where the criterion for dynamical instability is satisfied. We should note that the curve terminates before crossing the dotted line. This means that dynamical instability does not occur. Instead, as Boss (1986)
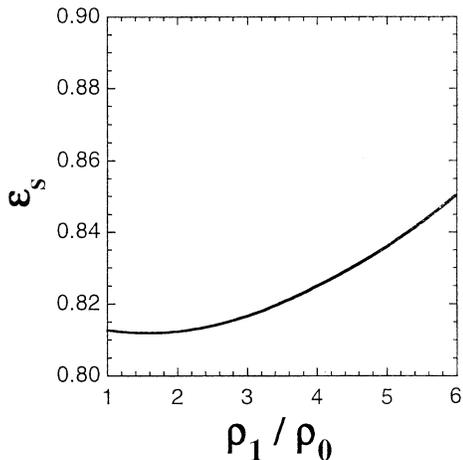
Fig. 12. The coaspect ratio where secular instability sets in for various density ratios ρ_1/ρ_0. The volume ratio V_1/V_0 is taken to be 1/8. The case where $\rho_1/\rho_0 = 1$ corresponds to the Maclaurin spheroid.

Table 1. The coaspect ratio where secular instability sets in for various volume ratios V_1/V_0. The volume ratio ρ_1/ρ_0 is taken to be 2. For the cases where $V_1/V_0 = 0$ and 1, the bodies become homogeneous spheroids, i.e., Maclaurin spheroids.

V_1/V_0	ε_s
0 (Maclaurin)	0.81267
1/8	0.812
1/3	0.816
1/2	0.816
2/3	0.815
1 (Maclaurin)	0.81267

pointed out, when the coaspect ratio exceeds the critical value ϵ_c, mass shedding from the equatorial plane may begin. In Fig. 12 we illustrate the variation of ϵ_s against ρ_1/ρ_0 in the case where $V_1/V_0 = 1/8$. The value of ϵ_s increases slightly and almost monotonically with ρ_1/ρ_0. In other words, as the degree of central condensation of mass increases the body becomes more stable against perturbations.

Finally, let us see the effect of the volume ratio V_1/V_0 on the criterion for instability. To save computational time, the numerical calculations are only executed for $V_1/V_0 = 1/8, 1/3, 1/2$, and 2/3. The results are summarized in Table 1 for the case of $\rho_1/\rho_0 = 2$. We can see from the table that the point where secular instability sets in does not depend strongly on the volume ratio V_1/V_0. It should be noted that, in all of the four cases, the equilibrium figures reach the critical coaspect ratio before the condition for dynamical instability is satisfied. However, in the limits of $V_1/V_0 \to 1$ and 0, we expect that dynamical instability occurs before reaching the critical coaspect ratio.

Therefore, it is concluded that the condition for secular instability is not eased compared to the Maclaurin spheroid even if inhomogeneity of the body is taken into account. Moreover, this condition does not strongly depends on the values of the parameters, V_1/V_0 and ρ_1/ρ_0. For the all cases we calculated here,

Table 2. The angular momenta needed for secular instability L_{secular} and for mass-shedding L_{critical}. The values are normalized by the total angular momentum of the present Earth-Moon system.

ρ_1/ρ_0	V_1/V_0	L_{secular}	L_{critical}
2	1/8	2.596	4.087
2	1/3	2.563	3.647
2	1/2	2.561	3.734
2	2/3	2.581	4.103
3	1/8	2.569	3.507
3	1/3	2.509	3.056

the body reaches the critical coaspect ratio ϵ_c before dynamical instability sets in.

5. Discussion

Now, let us apply our results to the rotational fission hypothesis of the lunar origin. We first consider what values of ρ_1/ρ_0 and V_1/V_0 are most suitable for the proto-Earth. As a first approximation, both the core and the mantle may be regarded to be homogeneous and their mean densities are about 4.51 g cm^{-3} and 10.8 g cm^{-3}, respectively. Therefore, for the value of ρ_1/ρ_0 of the present Earth we have

$$\rho_1/\rho_0 \sim 2.39 \quad . \tag{34}$$

If we consider the proto-Earth which was in the process of the core formation, then, the core density would be smaller than that of the present Earth. In this sense, the above value of ρ_1/ρ_0 is an upper limit. The ratio of the volume of the core to that of the present Earth V_1/V_0 is

$$\frac{V_1}{V_0} \sim 0.162 \quad . \tag{35}$$

Even if the volume torn from the magma ocean is taken into account, V_1/V_0 does not increase any more.

Thus, we can consider that for the proto-Earth ρ_1/ρ_0 was in the range between 1 and 2.39 whereas V_1/V_0 was in the range between 0 and 0.162. As we have seen before, for these ranges of the parameters ρ/ρ_0 and V_1/V_0, dynamical instability never occurs. Instead, mass shedding from the equator would occur if the proto-Earth had a sufficiently large angular momentum. The materials would be ejected from the equator to form a disk around the proto-Earth as Boss (1986) simulated numerically for a rapidly rotating proto-Earth with a polytropic density distribution of index 1/2.

The angular momenta needed for secular instability and for mass-shedding (i.e., where the system reaches the critical coaspect ratio) are tabulated in Table 2. As seen from this table, the magnitude of the angular momentum which is necessary to trigger mass shedding is at least three times as large as that of the present Earth-Moon system. However, if we consider that the values of ρ_1/ρ_0 and V_1/V_0 are within the ranges described above, the condition is almost the same as that for dynamical

instability of the Maclaurin spheroid. It seems very unlikely that the proto-Earth gained such a large amount of the angular momentum.

We thus conclude that rotational fission is an unlikely mechanism for lunar origin even if the inhomogeneity of the proto-Earth is taken account. Therefore, if the Moon was formed from the materials of the terrestrial magma ocean, we must look for another mechanism to strip the magma ocean and put enough material into suitable orbits.

References

Benz W., Slattery, W. L., Cameron, A. G. W., 1986, Icarus 66, 515

Benz, W., Slattery, W. L., Cameron, A. G. W. 1987, Icarus 71, 30

Benz, W., Cameron, A. G. W., Melosh, H. J., 1989, Icarus 81, 113

Boss, A. P., 1986, Icarus 66, 330

Boss, A. P., Peale, S. J., 1986, Dynamical Constraints on the Origin of the Moon. In: Hartmann W. K., Phillips R. J., Taylor G. J. (eds.) Origin of the Moon. Lunar and Planetary Institute, Houston, p. 59

Cameron, A. G. W., Benz, W., 1991, Icarus 92, 204

Chandrasekhar, S., 1969, Ellipsoidal Figures of Equilibrium. Dover Publications, New York, p. 78

Chandrasekhar, S., Lebovitz, N. R., 1962, ApJ 135, 248

Comins, N., 1979, MNRAS 189, 233

Durisen, R. H., Scott, E. H. 1984, Icarus 58, 153

Durisen, R. H., Gingold, R. A. 1986, Numerical Simulation of Fission. In: Hartmann W. K., Phillips R. J., Taylor G. J. (eds.) Origin of the Moon. Lunar and Planetary Institute, Houston, p. 487

Eriguchi, Y., Sugimoto, D., 1981, Prog. Theor. Phys. 65, 1870

Friedman, J. L., 1983, Phys. Rev. Letters, 51, 11

Friedman, J. L., Schutz, B. F., 1978, ApJ 200, 204

Imamura, J. N., Friedman, J. L., Durisen, R. H., 1985, ApJ 294, 474

Imamura, J. N., Toman, J., Durisen, R. H., Pickett, B. K., Yang, S., 1995, ApJ 444, 363

Okuchi, T., 1995, private communication (Master Thesis, Tokyo Institute of Technology)

Ringwood, A. E., Kato, T., Hibberson, W., Ware, N., 1991, Icarus 89, 122

Ringwood, A. E., Seifert, S. 1988, Luar Planet. Sci. XIX, 984

Tasssoul, J. L., 1978, Theory of Rotating Stars. Princeton Univ. Press, New Jersey, p. 271

Tasssoul, J. L. Ostriker, J. P., 1968, ApJ 154, 613